Acta Materialia 257 (2023) 119177

Contents lists available at ScienceDirect

Acta Materialia

journal homepage: www.elsevier.com/locate/actamat

Full length article

Rapid discovery of high hardness multi-principal-element alloys using a generative adversarial network model

Ankit Roy [a,*], Aqumar Hussain [c], Prince Sharma [b], Ganesh Balasubramanian [b], M.F.N. Taufique [a], Ram Devanathan [a], Prashant Singh [d], Duane D. Johnson [d,e]

[a] Pacific Northwest National Laboratory, Richland, WA 99354, USA
[b] Department of Mechanical Engineering and Mechanics, Lehigh University, Bethlehem, PA 18015, USA
[c] Department of Computer Science and Engineering, Ramaiah Institute of Technology, Bengaluru, Karnataka 560054, India
[d] Ames National Laboratory, United States Department of Energy, Iowa State University, Ames, IA 50011, USA
[e] Department of Materials Science & Engineering, Iowa State University, Ames, IA 50011, USA

ARTICLE INFO

Keywords:
Multi-principal element alloys (MPEAs)
Generative adversarial network (GAN)
Neuralnetwork (NN)
Hardness
DFT
Experimentation

ABSTRACT

Multi-principal element alloys (MPEAs) continue to gain research prominence due to their promising high-temperature microstructural and mechanical properties. Recently, machine learning (ML) and materials informatics have been used extensively for screening MPEAs, however, most of these efforts were focused on constructing classification and regression models for predicting phase stability and mechanical properties of known compositions. These approaches may accelerate the screening process but optimizing new compositions with desirable properties within a practical time frame from an infinitely large design space of MPEA systems remains a grand challenge. To tackle this composition optimization challenge, a *generative adversarial network* coupled with a neural-network ML model was utilized to design MPEAs by filtering compositions that have high hardness. Even in a high-dimensional space with 18 elements as descriptors, the ML model was able to generate optimized compositions from which one composition was found to have 10% higher hardness (941 HV) than the maximum in the training data (857 HV). Density-functional theory was used to provide thermodynamic and electronic insights to higher hardness of the new MPEA found. The present work can optimize compositions from a wide design space of 18 elements (including W, Ta and Nb) that presents an opportunity to synthesize new compositions for applications ranging from corrosion-resistant alloys to nuclear materials. The findings suggest that generative ML can greatly accelerate materials discovery by identifying novel compositions, which can serve as a data-informed tool to guide experiments.

1. Introduction

The concept of high-entropy alloys (HEAs), first conceived in 2004 primarily by two groups [1,2], was originally defined as an amalgamation of 5 or more elements in 5–35% atomic concentrations. Since its inception, HEAs have transformed the alloy research with an exponential rise in the number of related papers in the last decade. This can be attributed to their outstanding structural properties, such as excellent hardness [3], high-temperature strength [4], high elastic moduli [5] and corrosion resistance [6,7] that take place due to the core effects [1] like high entropy [1], sluggish diffusion [8,9], lattice distortion [10] and alloying. However, now this field has branched into a number of subgroups, the major ones being multi-principal-element alloys (MPEAs) [11] and complex concentrated alloys (CCAs) [12] that include materials with just 3 elements and in concentrations more than 35 atomic percent. A previous report [13] mentions that considering the 75 stable elements in the periodic table, if every 10% concentration change yields a new MPEA, then with 3–6 principal elements, over 592 billion new MPEAs can be made. This is an overwhelming number to deal with using Edisonian approaches via experimentation or even computations[9, 14–18]. Such a scenario calls for the use of modern data-centric techniques to explore the entire compositional landscape of MPEAs.

Given the cosmically large search space of unexplored alloy bases, experimentation and simulations alone cannot span the possible compositional space. Even though the field is two decades old, the number of alloys explored are only in the order of 1000 [19]. Under such

* Corresponding author at: Pacific Northwest National Laboratory, Richland, WA 99354, USA.
E-mail address: ankit.roy@pnnl.gov (A. Roy).

https://doi.org/10.1016/j.actamat.2023.119177
Received 19 October 2022; Received in revised form 17 July 2023; Accepted 21 July 2023
Available online 22 July 2023

a circumstance, use of data-driven machine-learning (ML) techniques, becomes compelling to facilitate a swift discovery of MPEAs. The use of ML for surfing through MPEA compositions began by the second half of the last decade with a notable work by Islam et al. [20] being the first to convert Hume-Rothery rules into numerical descriptors. In the subsequent years, there was a steep ascent in ML efforts for exploring new MPEAs that include interesting works like [20–28]. While ML has been successfully used in prediction/interpolation problems with higher accuracy when tested within the limits of the training set, most ML models lose accuracy when tested with datapoints that fall outside the bounds of training set. Although there are over a 100 works related to ML in MPEAs, most models have mainly focused on constructing regressor algorithms for either classifying phases or predicting mechanical properties, like hardness, yield stress or elastic modulus [24–26,29–31] while very few [32,33] have focused on the generation and optimization of new MPEA composition.

Considering the problem described above, a *generator-regressor* combination was adopted to find novel MPEAs with high hardness. Generative adversarial networks (GANs), proposed by Goodfellow et al. [34], have been used for medical image generation [35] and astrophysical image painting [36]. The specialty of GANs lies in its ability to learn from descriptors of existing MPEAs and produce statistically congruent compositions, similar to training data.

GANs have been employed here to predict new MPEA compositions by using an initial dataset of alloy compositions and hardness as input. An extensive search using GAN on 18-dimensional design space of Co-Fe-Ni-Si-Al-Cr-Mo-Ti-Nb-V-Zr-Mn-Cu-Sn-Ta-Hf-W-Zn MPEAs was performed. The new compositions synthesized by GAN become the search space from which the compositions with highest hardness were down-selected using a neural network (NN) regressor. This search resulted in the identification of two compositions with significantly higher hardness (>900 HV), which are better than known MPEAs rich in 3*d* transition metals. In validation, the predictions showed good agreement with Vickers microhardness measurements. Thermodynamic and electronic-structure analysis was performed on two candidate alloys with the highest hardness using density-functional theory (DFT) to gain electronic insights. The microstructural and microchemical characterization of the same was also done to understand the microstructural origin of exceptional mechanical response.

The methodology adopted in the present work differs considerably from the past works of similar nature. Ref. [32] found new compositions based on AlCoCrFeMnNi alloys by using a simulated annealing (SA) algorithm where the concentration of every element was limited between 5 and 35%. Authors discovered new compositions, but the highest predicted hardness was 650 HV that was limited by the upper bound to Al-Co-Cr-Fe-Mn-Ni family of alloys. In contrast, the present work includes a higher descriptor dimension of 18 elements with predicted hardness of 941 HV, which is 50% higher than known alloys in the training set or previously known works. Inverse projection (IP) is another approach that was applied into Fisher model to identify a high-performance zone in the Fisher plot that reverse calculated the features in the original space [37]. This approach predicted some compositions that would yield the high value of target properties, e.g., hardness. Then the authors [34] designed virtual compositions of Al-Co-Cr-Cu-Fe-Ni (and derivates) family of alloys by varying the elemental concentration between 5 and 35% and identified HEAs that lie in the high-performance zone of the Fisher plot. Their primary focus was on vanadium containing HEAs and the alloy with highest hardness was Co-Cr-Fe-Ni-V based. Ref. [38] developed an XGBoost model to predict hardness and studied the effect of Ta addition by increasing the Ta content in virtually formulated Ti-Zr-Nb-Ta alloys. They concluded that with addition of Ta the hardness should increase until a peak value and then decrease on further Ta addition. Ref. [39] and ref. [40] both built hardness screening models using neural network and genetic algorithms, respectively, with primary focus on Al-Co-Cr-Cu-Fe-Ni HEAs and their sub-groups. Another noteworthy work [33] that successfully found novel high hardness compositions used a support-vector regression model with a Radial Basis Kernel as the screening model and self developed an algorithm for formulating new compositions. Their algorithm generated $Al_xCo_yCr_zCu_uFe_vNi_w$ compositions by keeping the limits as: $15.0 < x < 47.0$, $5.0 < y < 22.0$, $6.0 < z < 34.0$, $5.0 < u < 16.0$, $5.0 < v < 31.0$ and $5.0 < w < 22.0$ at.%. The new compositions were then passed into the support-vector regression screening model and 35 new compositions were found with a higher hardness than the maximum in the training set. Very recently, Bayesian techniques have been leveraged for optimizing multiple constraints like solidus temperature, solidification range, thermal conductivity, density, ductility and yield strength [41]. The authors connected Bayesian classification with Bayesian optimization loops and identified a set of 21 compositions based on Mo-Nb-Ti-V-W alloy family that satisfied the strength-ductility objective. Further experimental investigation of these alloys was recommended serving as a swift tool for guided experiments to discover novel materials for gas turbine engine blade applications [41]. Another multi-objective constraint satisfaction framework that is agnostic of the composition was developed recently [42] to identify alloys with multiple optimized properties like hardness and strength [43].

Despite several previous efforts in predicting hardness, it may be emphasized that this work stands out for two primary reasons. First, the descriptor space encompasses a total of 18 elements (Co-Fe-Ni-Si-Al-Cr-Mo-Ti-Nb-V-Zr-Mn-Cu-Sn-Ta-Hf-W-Zn) of the periodic table which spans a larger composition space than all previous works. The possible new composition is not limited to Al-Co-Cr-Cu-Fe-Ni family of HEAs. Second, the power of ML is harnessed to generate new compositions by utilizing the statistical capabilities of GAN. The algorithm replicates the patterns existing in the training set to predict new compositions. The previous works either manually formulated the compositions or used mathematical algorithms to vary the elemental concentration in steps of 1–5 at.% to predict new ones. Along with above outlined reasons, the present approach is more time efficient in terms of computational efficacy, as it bypasses the need to exhaustively check compositions which have a low probability of showing high hardness. Moreover, the approach used here is fully autonomous with minimal to no human interference, as needed for stepwise-composition search algorithms. This makes artificial intelligence (AI) driven GAN approach more capable of improvement as AI capabilities improve in the future.

1.1. Methodology

1.1.1. Data generation by GANs

The basic principle of GANs are derived from the Nash Equilibrium [44] in game theory with two main competitive networks comprising of the generator *G* and the discriminator *D*. A point in latent space serves as input for the G which then uses it to produce an output data subject to the distribution of the original real data. Therefore, now there are two categories for the dataset: the real data (x) and the generated data. Following this, the competitive network D is trained such that it distinguishes between the generated data and the real data by assigning the numeric value 1 to real data and 0 to the data generated from G [45]. Simultaneously, G is trained such that it can generate data that would be most likely be classified with numeric value 1 by the D. With an objective of winning the game, the two networks constantly optimize themselves to make their generation and discrimination abilities more accurate, until Nash equilibrium is established between the two networks.

The flowchart in Fig. 3 shows the structure and working of GAN. The generator takes random variables (y) as input and generates new samples G(y) mimicking a similar distribution as in the real data. Both real data x, and generated data G(y) serve as input to the discriminator D, which should classify real data to be true and label it with value 1 while generated data is labeled false with value 0 [46]. D is trained such that the probability of classifying generated data G(y) from real data is maximized. On the other hand, the generator is trained such that it

minimizes the probability of a generated data being labeled with zero, i.e., minimize the function log (1 – D(G(z))).

1.1.2. Learning and training methodology

The training of the discriminator involves the optimization of an objective function expressed as follows [45,46]:

$$Obj^{D}(\theta_D, \theta_G) = -\frac{1}{2}E_{x\sim p_{data}(x)}[logD(x)] - \frac{1}{2}E_{z\sim p_z(z)}[\log(1 - D(g(z)))] \quad (1)$$

Where $Obj^{D}(\theta_D, \theta_G)$ is the objective function, θ_D and θ_G are the two terms on the right-hand side of the equation respectively, D (x) denotes the probability of x sampled from the real data instead of generated data, and E represents the expectation. Since the training data consists of real data distribution ($p_{data}(x)$) and generated data distribution ($p_g(x)$), it is required to minimize the objective function of the generator given in Eq. (1). To do so, Eq. (1) is rewritten as [45,46]

$$Obj^{D}(\theta_D, \theta_G) = -\frac{1}{2}\int_x p_{data}(x)\log(D(x)dx - \frac{1}{2}\int_z p_z(z)\log(1 - D(g(z))dz$$

$$= -\frac{1}{2}\int_x p_{data}(x)\log(D(x))dx - \frac{1}{2}\int_z p_g(x)\log(1 - D(x))dx. \quad (2)$$

Here p_g (x) denotes the distribution of generated data. For form $-a\ log(f) - b\ log(1 - f)$, the minimum occurs at $f = \frac{a}{a+b}$. By analogy, Eq. (2) achieves its minimum at [45–47]

$$D_G^*(x) = \frac{p_{data}(x)}{p_{data}(x) + p_g(x)}. \quad (3)$$

$D_G^*(x)$ is the optimal solution of discriminator D. Putting D* from (3) into (2) is a problem of finding the minimum of Jensen-Shannon divergence (JSD) between $p_{data}(x)$ and $p_g(x)$ and the JSD achieves a minimum when the two are equal [47]. Simply put, Eq. (3) reaches a minimum when $p_{data}(x) = p_g(x)$, which signifies that the generative model perfectly replicates the real data distribution in the generation process.

1.1.3. Hardness prediction by neural networks

Artificial neural networks are computer algorithms that replicate a human brain's neuron network [48]. They consist of an input layer, output layer and several hidden layers. Each node is like a neuron which is linked to other neurons. Each neuron has a certain threshold and weight. Below a fixed threshold the neuron remains inactive, but it is activated beyond the threshold input it starts transferring data to the next layer. The hardness prediction is done by a regression NN the architecture of which is depicted in Fig. 1. The hyperparameters of the NN need to be optimized for the highest predictive accuracy and, after iterating the training in a range of hyperparameters, the best ones were found to be as follows: batch size = 32, learning rate = 0.5, number of hidden layers = 4, maximum number of nodes in the hidden layer = 32.

A major limitation associated with any ML model is the variability of model output with the change in model parameters like the learning rate and number of layers. Ref. [29] discussed the variation in accuracy of phase classification with different combination and number of features. However, the change became insignificant beyond four descriptors, therefore, they selected a four-descriptor model with highest accuracy to conclude their findings. This process is often defined as parameter optimization (as described above) that is a widely accepted approach in the material design community.

The implementation of NN requires the specification of an activation function which is basically a mathematical function that converts a given input into the required form of output within some bounds. This output is the total weight with a bias added to it and its value determines whether the neuron is to be activated or not. The goal of the activation function is to introduce non-linearity to the neuron's output which would have otherwise behaved like a linear regression model with a significantly low learning power. The two most popular activation functions are the Rectified Linear Unit (ReLU) [49] activation function and the Scaled Exponential Linear Units (SELU) [50]. The ReLU is expressed as $f(x) = \max(0, x)$, which means it outputs the input as is when the input is positive and outputs a value of 0 otherwise. Whereas the SELU [50] is expressed as

$$f(x) = \lambda x \ if \ x > 0 \quad (4)$$

$$f(x) = \lambda\alpha(e^x - 1) \ if \ x \leq 0 \quad (5)$$

Here, $\lambda = 1.5$ and $\alpha = 1.67$. Although both ReLU and SELU were tried in this work, a better prediction accuracy was obtained with SELU and hence SELU was adopted for the final model. SELU has been found

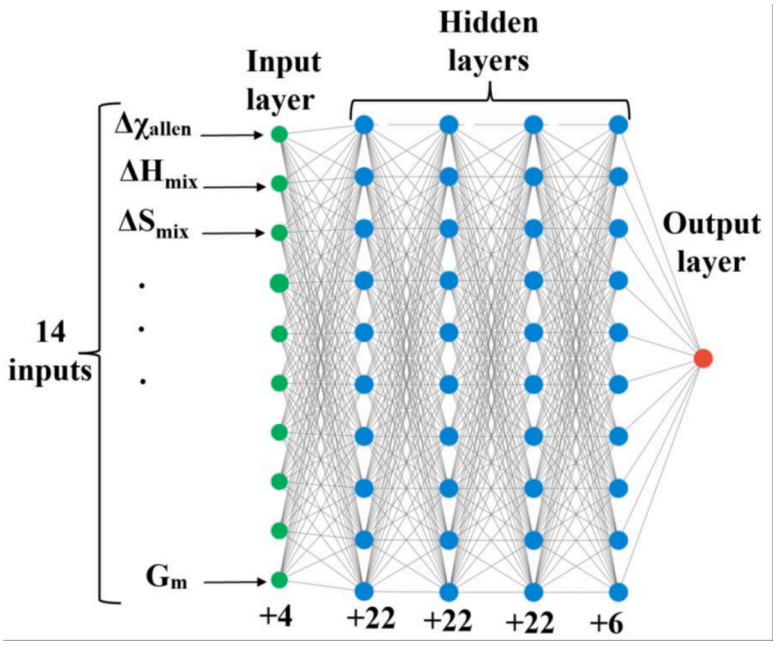

Fig. 1. Architecture of the NN regressor used for predicting the hardness values. The $+x$ notations at the bottom represent the additional nodes that are not shown in the schematic.

to be more accurate in other prior works where NN was used to predict phases of HEAs [51].

The number of input nodes is equal to the number of descriptors (14) and there is only one output node, which is the hardness value. Note that 11 out of the 14 descriptors are adopted from our previous work on Young's modulus predictions [25], where the new descriptors added here are Pauling's electronegativity, difference in shear moduli, and average shear moduli. To explain the significance of the inclusion of shear modulus (G), we refer to the relations between hardness and G that were established previously [10]. Under an externally applied strain, the hardness (H) represents the tendency of a material to resist local plastic deformation, before gliding takes place [52,53]. In the presence of a solute atom with a different atomic radius than the host species, a stress field is induced due to the resulting local compression or expansion of the lattice. These stress fields interact with the dislocations giving rise to a dislocation interaction energy denoted by U_{size} that is positive when the solute is larger than the host and is expressed as $U_{size} = \frac{4(1+\nu)Gbr^3\varepsilon_b sin\theta}{3(1-\nu)R}$ [54], where G is shear modulus, b is the magnitude of the Burger's vector, R is the distance between the dislocation core and solute atom, θ is the angle between the slip direction and the line connecting the dislocation core and solute atom, r is the radius of solvent atomic and r $(1+\varepsilon_b)$ is the solute atom radius where $\varepsilon_b = \frac{1}{a}\frac{da}{dc}$, a being the lattice constant, c being the solute concentration and ν is Poisson's ratio. Hence, to integrate the ML model with the physics that underlies the hardness of a material, the shear modulus (G) descriptors are included along with the other set of descriptors, as shown in Table 1.

An initial data analysis is performed by quantifying the existing correlations between any given pair of descriptors. This is done by calculating the Pearson correlation coefficient P, where $P = 1$ and P=–1 denote a strong positive and negative correlation respectively. The heat map in Fig. 2 shows that all pairs have low correlation except average lattice constant (a_m) with the difference in lattice constants (Δa_m) that have a high correlation of 0.9. However, none of these were excluded from analysis as there was no full correlation. In the present study, it will be revealed later using Shapley Additive exPlanations (SHAP) [55] that both features contribute unequally to model performance. Additionally, since the average lattice constant (a_m) and the difference in lattice constants (Δa_m) have different mathematical expressions, they might have a lower correlation coefficient if the composition space is varied significantly. To avoid the risk of rendering the model agnostic of a significant and relevant feature in the event of an updated composition space, both average lattice constant (a_m) and the difference in lattice constants (Δa_m) have been included. Thus, a priori elimination of any feature can be detrimental to predictive power.

Table 1
List of descriptors used for hardness prediction in this work.

Descriptor	Description
$\boldsymbol{\Delta\chi_{Allen}} = \sqrt{\sum_{i=1}^{n} \boldsymbol{C_i}(\chi_i - \overline{\chi})}$	Difference in Allen electronegativity
$\boldsymbol{\Delta\chi_{Pauling}} = \sqrt{\sum_{i=1}^{n} \boldsymbol{C_i}(\chi_i - \overline{\chi})}$	Difference in Pauling electronegativity
$\boldsymbol{\Delta S_{mix}} = -\boldsymbol{R}\sum_{i=1}^{n}(\boldsymbol{C_i ln C_i})$	Mixing entropy
$\boldsymbol{\Delta H_{mix}} = \sum_{i=1, i\neq j}^{n} \boldsymbol{4H_{ij}C_iC_j}$	Mixing Enthalpy
$\boldsymbol{\delta} = \sqrt{\sum_{i=1}^{n} \boldsymbol{C_i}\left(1 - \frac{r_i}{\overline{r}}\right)}$	Difference in atomic radii
$\boldsymbol{\Delta a} = \sqrt{\sum_{i=1}^{n} \boldsymbol{C_i}(a_i - \overline{a})^2}$	Difference in lattice constants
$\boldsymbol{\Delta T_m} = \sqrt{\sum_{i=1}^{n} \boldsymbol{C_i}(T_i - \overline{T})^2}$	Difference in melting temperatures
$\boldsymbol{\lambda} = \frac{\boldsymbol{\Delta S_{mix}}}{\boldsymbol{\delta^2}}$	A geometrical parameter
$\boldsymbol{\Omega} = \frac{\boldsymbol{T_m \Delta S_{mix}}}{\boldsymbol{\lvert\Delta H_{mix}\rvert}}$	Parameter for predicting solid state formation.
$\boldsymbol{T_m} = \sum_{i=1}^{n} \boldsymbol{C_i T i}$	Average melting temp calculated by rule of mixture.
$\boldsymbol{a_m} = \sum_{i=1}^{n} \boldsymbol{C_i a_i}$	Average lattice constant calculated by rule of mixture.
$\boldsymbol{V.E.C} = \sum_{i=1}^{n} \boldsymbol{C_i}(V.E.C)_i$	Average valence electron composition calculated by rule of mixture.
$\boldsymbol{\Delta G} = \sqrt{\sum_{i=1}^{n} \boldsymbol{C_i}(G_i - \overline{G})^2}$	Difference in Shear moduli
$\boldsymbol{G_m} = \sum_{i=1}^{n} \boldsymbol{C_i G_i}$	Average Shear modulus calculated by rule of mixture.

The dataset of 241 alloys was divided into 200 for training and 41 for testing. This procedure was iterated four times to distill four different and random test sets and check for the variability in mean absolute error (MAE) and mean squared error (R^2) of predicted versus experimental hardness data. One random case from these iterative cycles was chosen and the predictions versus the experimental values of hardness were plotted to visualize the accuracy of predictions in the results section. The MAE varied between 36 and 40 HV and R^2 varied between 0.95 and 0.99 for these iterations, showing that model training is stable and does not vary largely when the training and testing sets are randomly distributed in each iteration from the original dataset.

1.1.4. Density functional theory (DFT) calculations

The DFT-based Korringa-Kohn-Rostoker (KKR) Green's function method combined with the coherent potential approximation (CPA) was used to calculate phase stability, bulk moduli, and electronic structure of predicted MPEAs [56,57]. The DFT-KKR-CPA performs configurational averaging simultaneously with DFT charge self-consistency, which properly includes alloy-induced Friedel impurity-charge screening. The core electrons were treated fully relativistically (includes spin-orbit coupling) and the semi-core/valence electrons were treated scalar relativistically (i.e., neglecting spin-orbit coupling). The self-consistent charge density was obtained from the Green's function using a complex-energy contour integration and Gauss-Laguerre quadrature [56]. The Perdew-Burke-Ernzerhof (PBE) exchange-correlation functional was used in all calculations [58]. A site-centered spherical-harmonic basis including *s, p, d,* and *f*-orbital symmetries (i.e., $L_{max} = 3$) with equally spaced *k*-space mesh (18 × 18 × 18) was used for Brillouin zone integrations.

1.1.5. Experimental validation

Four GAN predicted alloys with highest hardness values were synthesized by arc melting compressed pellets in an inert argon atmosphere with required ratios of high purity powders (>99.95%) of Co, Fe, Ni, Al, Cr, Mo, Ti, Zr Ta and W from Sigma-Aldrich. To ensure composition homogeneity each sample was overturned and re-melted five times. The melted sample was cut from center and polished with 1200 grit paper followed by diamond and fine silica to prepare sample for Vickers microhardness and SEM imaging. Vickers microhardness was performed using LECO LM248 with 100 gmf load, the final values calculated from the mean of 10 independent measurements per sample. Hitachi 4300SE/N Scanning Electron Microscope (SEM) equipped with energy-dispersive spectroscopy (EDS) comprising of an Octane Elect Plus Silicon Drift Detector and TSL High speed Hakari EBSD camera, was utilized for microstructure, elemental, and phase analysis.

1.1.6. Workflow pipelines

The integrated flowchart coupling all the individual steps is shown in Fig. 3. Data was collected manually from the literature for the alloy compositions with their hardness values, as described previously [25]. With the goal of generating new alloy compositions by learning the patterns in the existing dataset, a table was constructed with all the elements (total 18) used in our dataset listed in adjacent columns. The atomic percent of each metal used for a given alloy was extracted and populated in the table as shown in step 1 of Fig. 3. The completed table is used as an input or the training set for the GAN which then outputs a similar table but with new compositions that are synthesized out of the same list of metals that was supplied to it. The overall mean atomic percent of each element in all the GAN generated alloys combined is somewhat close to that in the originally supplied data (training data). For example, if all the 241 alloys in the training data had an overall mean of 23% Fe in them (alloy 1 has 15% Fe, alloy 2 has 35% Fe and Alloy N has 20% Fe, hence all N alloys have an average 23% Fe) then the

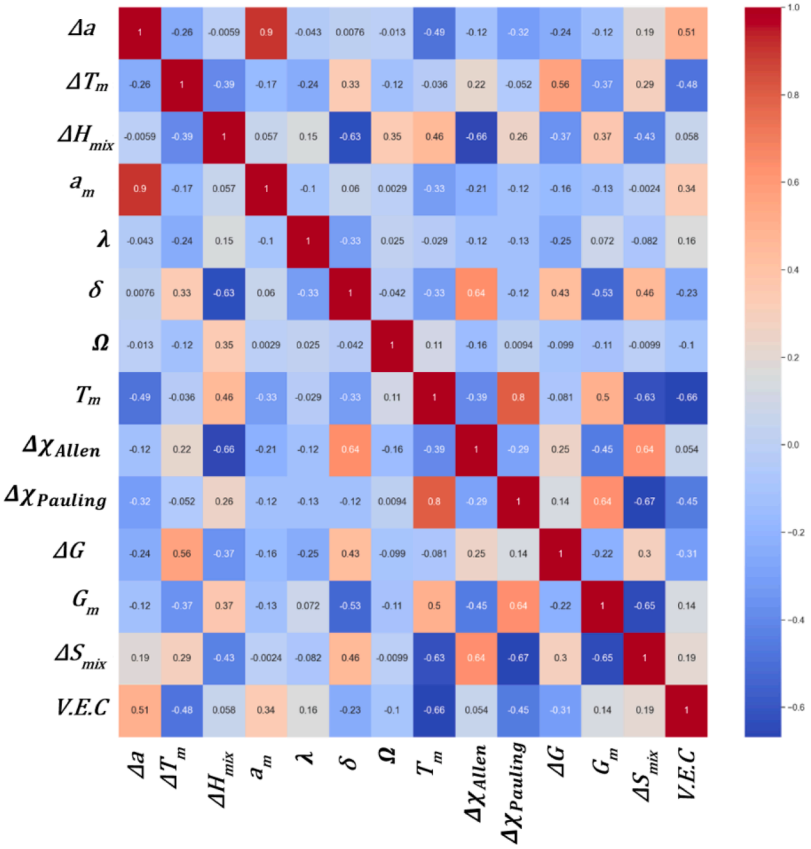

Fig. 2. Heat map displaying the correlation values between the descriptors of the dataset with $P = 1$ denoting strong positive correlation and $P = -1$ denoting strong negative correlation.

new 200 alloys generated by GAN have a mean around 20–25% Fe. Therefore, GAN maintains the mean atomic percent integrity between the training data and generated data. After the generation of 200 new compositions, we proceed to step 2.

In step 2, a table was constructed with the same 241 alloys used in step 1 and then the chemical signatures or the fingerprints were determined that govern the target property i.e., hardness. The fingerprints were expressed in terms of mathematical equations as shown in Table 1, following which an inhouse python code was developed that calculates all the 14 descriptors and outputs their values, by taking only the alloy composition as the input as shown in step 2 of Fig 3. This dataset with the thermodynamical, physical, and atomic descriptors was used as the training data for the NN regressor which is then trained to predict the hardness of any given unknown alloy. The dataset was split such that 200 data are in training set and 41 in the test set. The testing accuracy is visualized by comparing the predicted values to experimental hardness of 41 alloys that were used as the test set. This NN regressor will be used in step 3 to predict the hardness of all the new alloys generated by the GAN in step 1.

In step 3, the alloy compositions generated by GAN in step 1 are then supplied to our inhouse code to calculate the 14 descriptors. This dataset of 200 GAN generated alloys along with their 14 thermodynamic and atomic descriptors are then passed into the NN as a test set, which outputs their hardness values. Two alloys with the highest hardness are then filtered out from the set of 200 and lab tested for their experimental hardness.

2. Results and discussion

The mean atomic percent of every element in the training data (241 alloys) for GAN is compared with the output or synthesized compositions generated by GAN. Fig. 4(a) compares the mean atomic percent of each element, and it was found that there is very little difference in the overall mean atomic percent of the elements between the training and the generated data. This shows that the GAN generates new alloys within the upper and lower compositional bounds of each element from the training data.

In Fig. 4(a), as Si, Mn, W and Zn are some of the least occurring elements in our training set, GAN does not get enough training to synthesize new compositions with a significant presence of these elements. Therefore, the GAN synthesized data hardly contains any composition with these elements and hence the GAN comparison bar (Fig. 4(a)) is missing for these elements. Other elements like Mo, Ti, Fe and Cr have a significant frequency of occurrence in the training set and thus the GAN synthesized data also contains a similar distribution of these elements, as seen by similar lengths of the comparison bars for these elements. Further analysis, using box-and-whisker plots in Fig. 4 (b) and (c), shows a similar distribution for the original and GAN generated data. The elements like Co, Ni, Al and Cr with a high frequency of occurrence in the training data have a closely replicated distribution in the GAN data as visible by closely matching sizes of the box and whiskers of these elements. On the contrary, elements like Mo and Ti that have a relatively low frequency of occurrence have considerable smaller box and whisker size in GAN generated data. Although GAN tried to produce Mo and Ti data in a way that they have outliers (data lying outside (1.5× interquartile range), denoted by red +) as that in the original data. This shows the ability of GAN to closely replicate individual data patterns from original data. Only Co, Fe, Ni, Al, Cr, Mo, Ti and Cu are shown in the box-and-whisker plots as the occurrence and number of data points for the other elements was too low.

Naturally, one would think that if the objective is to find alloys with high hardness, the training data should include many refractory alloys.

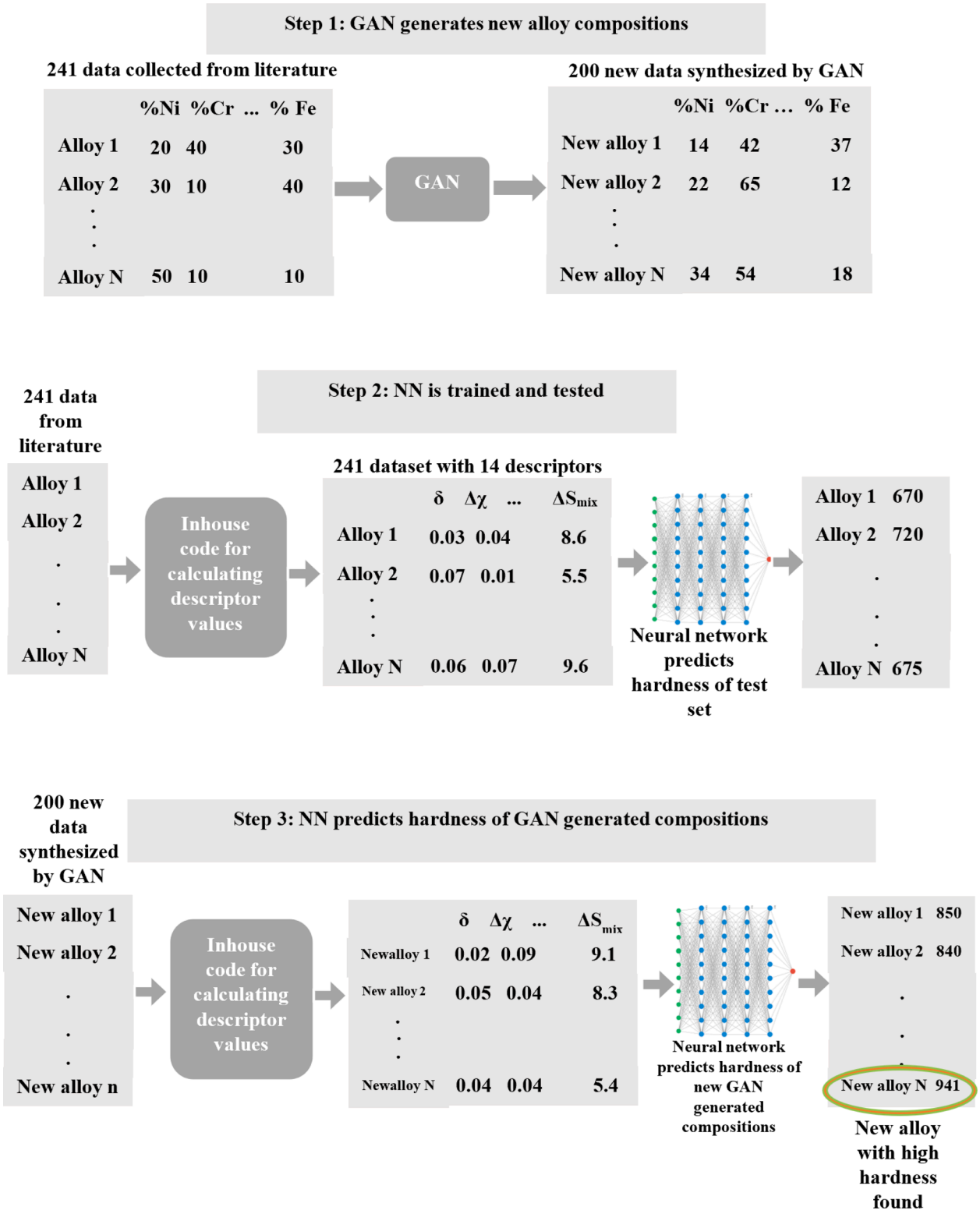

Fig. 3. Flowchart: Steps to generate new alloy compositions using GAN and then filtering out promising ones with high hardness using a NN model trained on experimental data.

The major limitation on the reliable use of ML in materials science community today is the sparsity of relevant data. Such is the limitation faced in our work too due to which it was attempted to curate the available alloy hardness data from the literature. It was particularly found that the open literature has a relatively small number of refractory MPEAs as compared to those containing the Cantor alloy elements (Cr, Mn, Fe, Co and Ni).

The NN predicted hardness values shown in Fig. 5 are in good agreement with the experimental values with the line of fit $y = 0.99x$ (intercept set to 0) with a MAE = 38.9 HV and $R^2 = 0.98$, which is almost superimposed on the $y = x$ line. The line in Fig. 5 is shown with intercept set to 0 because the ML model predictions approach 0 when the

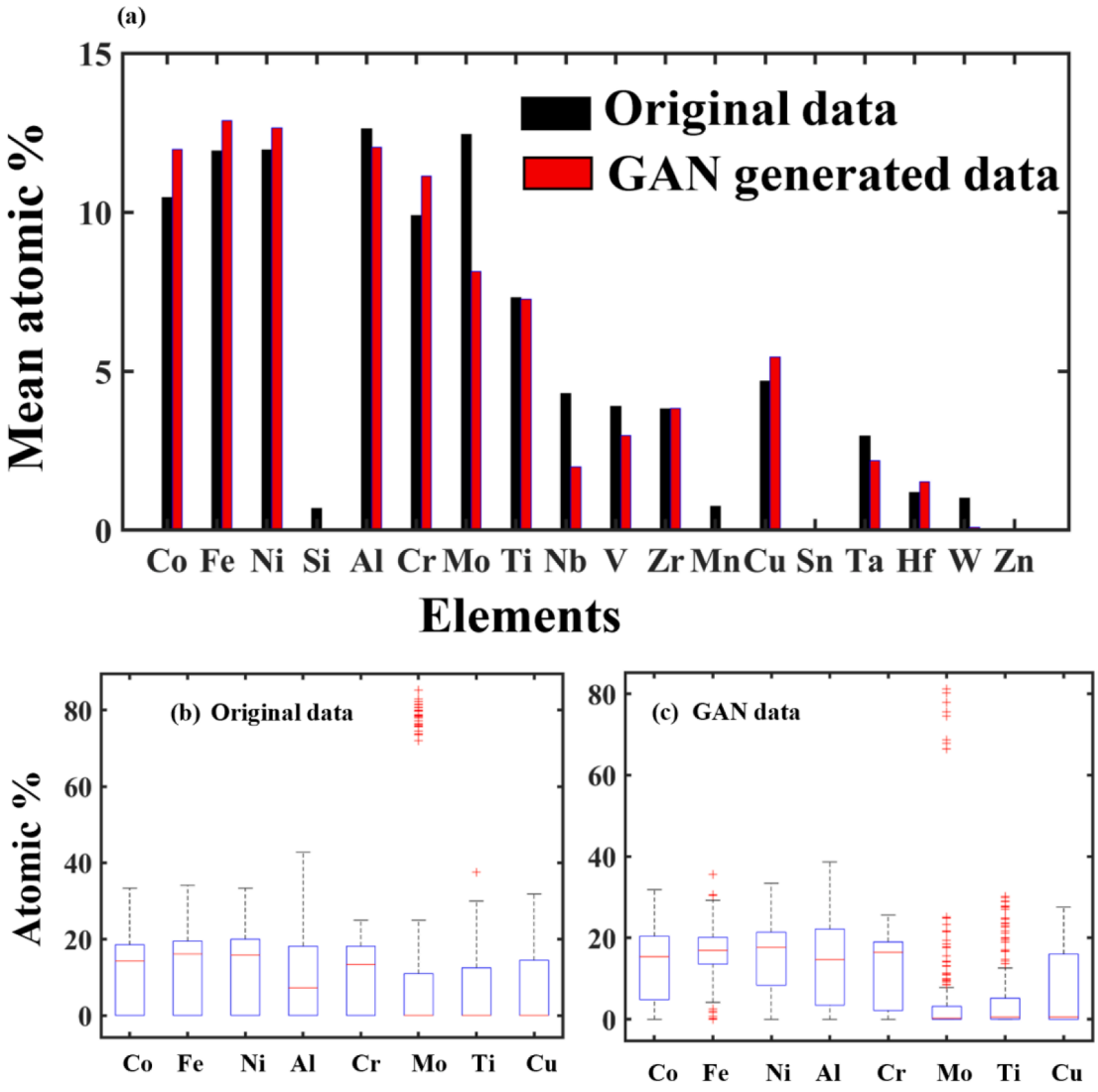

Fig. 4. **(a)** Elemental mean atomic percent in the training data compared to that in GAN data. The highest variation is seen in Mo while the least in Zr. **(b)** Box-and-whisker diagram of select elements from the original training dataset. **(c)** Box-and-whisker diagram of select elements in the GAN generated data.

experimental hardness approaches 0 HV. We note that the R^2 value for the NN with RELU was 0.88 (with intercept 0), therefore the SELU was adopted as mentioned in the methods section. Establishing the accuracy of our NN regressor means that it is now well-trained and ready to predict hardness of the 200 new compositions generated from the GAN with sufficient accuracy.

The SHAP analysis in Fig. 6(a) shows the effect of each individual data point and its descriptors on the model prediction. Every dot in Fig. 6 (a) is a sample point where the ordinate denotes the descriptors used and the abscissa represents its SHAP value of the datapoint for that descriptor. The significance of a particular descriptor can be assessed by the horizontal spread of its data along the abscissa. The wider the spread of the data, the higher is the contribution of the descriptor. The overall feature importance is shown in Fig. 6(b) where the VEC has the highest importance in determining the hardness of an alloy. These predictions are in good agreement with previous hardness prediction [37,59], where the authors reasoned that while VEC plays an important role in phase formation [60] (FCC is promoted for VEC $>$ 8 while BCC is preferred for VEC $<$ 7) it indirectly also determines hardness because generally high hardness can be achieved by promoting the BCC phase. Zhang et al. [59] also shown that high ΔS_{mix} and low ΔH_{mix} are beneficial for improving hardness which is in line with the findings in Fig. 6(b). It was also noticed that G_m quite significantly effects the hardness. This observation can be supported by findings from our previous work [10] where it was found that the average shear modulus G_m is crucial in increasing the resistance to plastic deformation by increasing the solute atom-dislocation interaction energy thereby increasing the hardness.

The final step involves the testing of the 200 GAN-generated compositions using NN regressor. Notably, the NN regressor is a much faster technique compared to other computational simulations like MD and DFT. The NN regressor took less than 1200 *ms* to output the hardness of all 200 alloys, which is a massive increase the speed of alloy screening as compared to MD and DFT. Although one caveat is that the overall task of data curation, code development for descriptor calculation and NN training may demand several weeks of person hours. The hardness prediction using NN shows that more than 3 of the GAN-generated alloys have higher hardness than any other alloy in the training set.

Fig. 7 shows the hardness of all the 241 alloys in the training set (black circles) and that of the 200 GAN generated alloys arranged in the descending order. Note that the three GAN-generated compositions whose hardness were predicted to be higher than the hardest alloy (857 HV) in the training set. This shows that ML has the capability to generate new compositions that can outperform the properties of the training set and hence can serve as an ingenious tool to discover novel compositions. Two of the three novel compositions (with hardness higher than training data), along with 2 other GAN-generated alloys with high hardness are

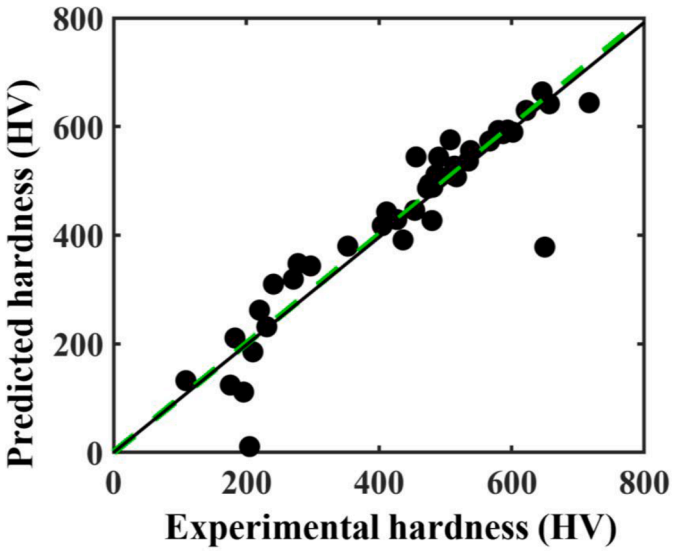

Fig. 5. The predicted versus experimental hardness values for the 41 alloys in the test set. The trendline $y = 0.99x$ (intercept set to 0) is denoted by solid-black line with a R^2 value of 0.98 and MAE = 38.9 HV. When the intercept is not set to 0, the equation is $y = 0.95x + 17.19$, with a R^2 value of 0.85. The $y = x$ line that corresponds to ideal case, where predicted hardness is equal to experimental hardness, is given by dashed-green line.

listed in Table 2. These four compositions were experimentally tested. These four included the top two compositions and then the 5th and the 7th from top. This selection was done to study the effect of inclusion of different principal elements in the alloys. As the 3rd and 4th had a similar composition to the 1st and 2nd, we skipped to the 5th and then 7th. As we go down our list, the principal elements change, though all alloys are formulated within the domain of the 18 elements used as descriptors for training the GAN.

The top-most composition exceeded the predicted hardness and thus demonstrates that ML can be successfully used to discover new compositions with properties exceeding that of the training set. Although the second composition fell below expectation in the experiments, it is still as hard as the hardest alloy in the training set (857 HV). Our inference is that GAN systematically generates a population of candidates with a

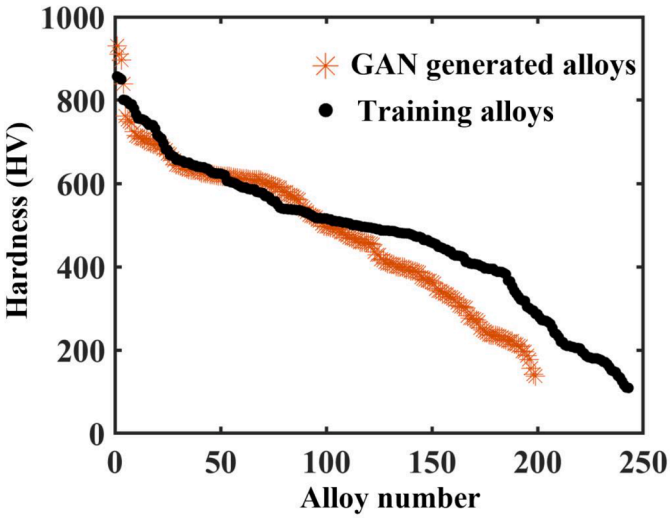

Fig. 7. Hardness of 200 GAN-generated alloys as predicted by NN (red asterisks) compared to the experimental hardness of the 241 alloys in the training set (black circles). 3 of the 200 alloys generated by GAN had a higher hardness than any other alloy in the training set.

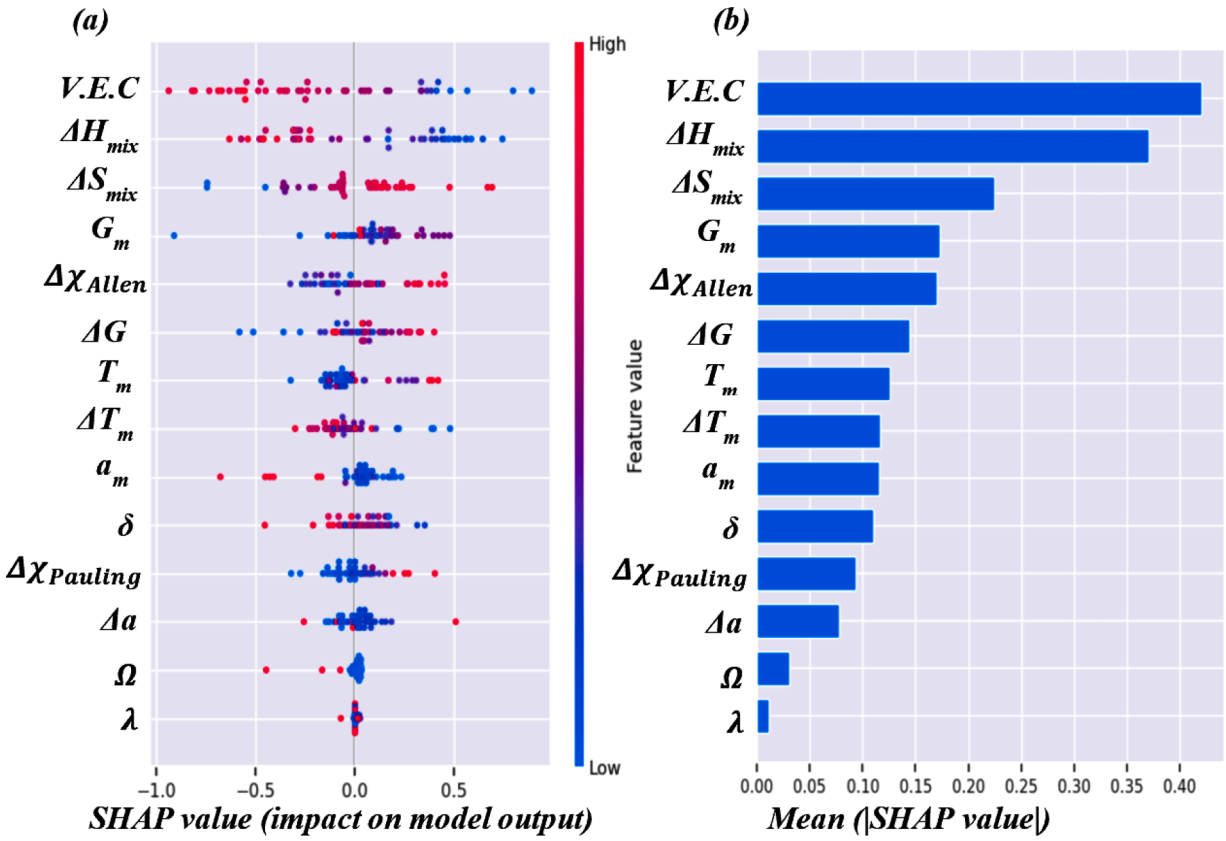

Fig. 6. Analysis of descriptor contribution by (a) SHAP value distribution of data points, and (b) feature importance ranked by decreasing order of importance.

Table 2
List of high-hardness compositions found by GAN. The hardness of the first composition exceeds the predicted hardness – harder than the hardest alloy (857 HV) in the training set.

#	Alloy	Predicted H (HV)	Experimental H (HV)
MPEA1	$Co_{14.86}Fe_{14.49}Ni_{15.18}Al_{17.31}Cr_{16.22}Mo_{21.52}Ti_{0.41}$	930	941 ± 13
MPEA2	$Co_{12.89}Fe_{10.89}Ni_{4.21}Al_{2.53}Cr_{8.31}Mo_{25.10}Ti_{30.23}Zr_{4.19}Ta_{1.09}W_{0.38}$	910	858 ± 25
MPEA3	$Co_{0.24}Fe_{20.94}Ni_{19.58}Al_{21.57}Cr_{20.94}Mo_{13.17}Ti_{3.56}$	761	700 ± 9
MPEA4	$Co_{13.88}Fe_{17.18}Ni_{23.52}Mo_{21.71}Ti_{0.83}V_{22.77}$	749	713 ± 13

relatively high hardness representing a forced extrapolation of the training data. It can be seen from Table 2 that the experimental values are within 8% error from the predicted values. The low error margin shows that the method has the potential to accelerate the discovery of new materials with desired properties.

The variation of principal elements and their atomic percent in the alloys (listed in Table 2) demonstrate that our approach allows a detailed analysis of the effect of small composition variations in a reduced parameter space containing, for example, some minor elements like Ti, W, Ta and Zr. When moving from the first to the second alloy in Table 2, Ti was added as a principal with Zr, Ta and W in minor quantities. This variation caused a significant drop in hardness as predicted by our NN and validated by experiments. In the 3rd composition the effect of Co removal caused a drop in the hardness and in the 4th, the addition of V and removal of Ti caused a further drop. Thus, the methodology serves as a guide tool for experimentalists, wherein, it is possible to fine tune the predictions by considering both major and minor compositional variations.

A comparative analysis of compositions with high hardness found from prior works is shown in Fig. 8. The composition of the alloy numbers marked on x-axis of Fig. 8 are given in Table 3. Clearly, most compositions except one found in prior works have hardness under 900 HV. The one exception being $Co_{18}Cr_7Fe_{35}Ni_5V_{35}$ with hardness 1148 HV from Ref. [37]. In the current work, the maximum hardness found was 941 HV which is lower than some high hardness alloys found using ML and mentioned in literature. But there are some striking points that are noteworthy in this case that are described in the subsequent paragraphs.

Most of the efforts attempting to find new compositions using ML, have trained the models only by using 5–10 elements in the training set as elaborated in Table 3. With fewer elements as compared to that in the present work (18), the ML model learns sufficiently well on the training set and is able to optimize the compositions adequately such that the output composition can exceed the hardness of those in the training set. The model in the current work is simultaneously dealing with optimizing 18 elements which drastically increases the number of variables and thus increases the level of complexity of the model. Additionally, the dataset size is limited to 241 which is similar or comparable to dataset sizes used in other works. Despite the large number of input descriptors, and small training data, the ML model is able to generate new compositions that exceed the maximum hardness of the training set by ~ 10% as shown in Table 3. It is acknowledged that the complications of adding more elements without a considerable increase in the dataset size is a probable cause of the model not being able optimize the composition to its full potential, thus only able to achieve and increase of 10% hardness in the optimized composition as compared to the training set.

Although the ML-generated alloys in this work are only 10% harder than that in the training set, the methodology offers a wider design window for formulating compositions from a palette of 18 elements as compared to a previously achieved 10 elements. For example, the choice to include elements like Ti offers room to increase resistance to corrosion and wear [61] and also increase the yield strength [62]. Inclusion of elements like Mo increases the compressive strength [63] and adds to the corrosion resistance of the alloys [64] by forming a protective passive layer. Elements like W, Ta and V allow for the design of nuclear and plasma facing materials [65]. Although the number of alloys with these elements is low in the dataset, the ML model is not completely agnostic of their role and effect, and includes them in the design space, thus allowing for future possibilities of optimizing compositions with these elements when the dataset includes more entries with W, Ta and V. By including 18 elements as features, the design space is kept wide and flexible for a large possibility of outputs depending upon the alloy application requirement, training data and the parameters used in training.

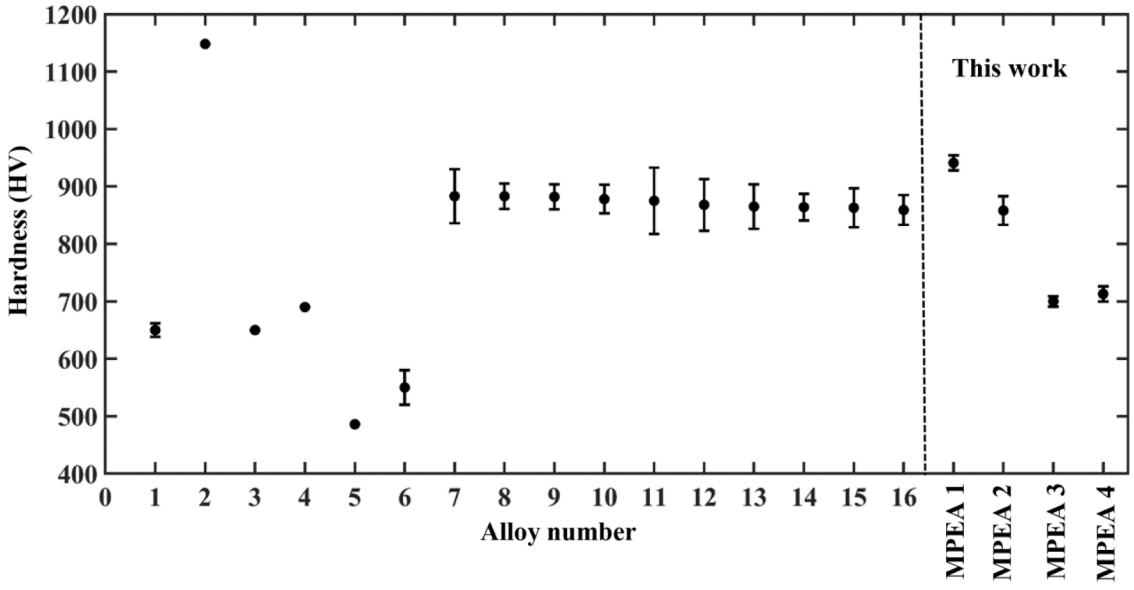

Fig. 8. Comparison of the compositions found in this work versus the ML obtained high hardness compositions in previous works.

Table 3
A list of ML obtained high hardness compositions in previous works.

Alloy no.	alloys	Max hardness obtained (HV)	Max hardness in training set (HV)	% increase in obtained hardness versus training hardness	Number of elements in the training data	Refs.
1	$Al_{24}Co_{18}Cr_{35}Fe_{10}Mn_{7.5}Ni_{5.5}$	650 ± 12	900	No increase	8	[32]
2	$Co_{18}Cr_7Fe_{35}Ni_5V_{35}$	1148				[37]
3	$Al_{20}Cr_5Cu_{15}Fe_{15}Ni_5Ti_{10}V_3$	650	920	25	10	
4	$Al_{21}Cr_{27}Fe_{29}Ni_5Mo_{18}$	690				
5	$Al_{28.56}Cr_{23.8}Fe_{23.8}Ni_{23.8}$	486	775	No increase	6	[39]
6	Ti-Zr-Nb-Ta	525 ± ~30	536	No increase	5	[38]
7	$Al_{43}Co_{22}Cr_{23}Cu_0Fe_7Ni_5$	883 ± 47				[33]
8	$Al_{47}Co_{20}Cr_{18}Cu_5Fe_5Ni_5$	883 ± 22				
9	$Al_{43}Co_{22}Cr_{22}Cu_0Fe_8Ni_5$	882 ± 22				
10	$Al_{47}Co_{19}Cr_{19}Cu_{05}Fe_5Ni_5$	878 ± 25				
11	$Al_{43}Co_{24}Cr_{22}Cu_0Fe_5Ni_6$	875 ± 58				
12	$Al_{43}Co_{25}Cr_{22}Cu_0Fe_5Ni_5$	868 ± 45	775	14	6	
13	$Al_{43}Co_{24}Cr_{23}Cu_0Fe_5Ni_5$	865 ± 39				
14	$Al_{43}Co_{18}Cr_{20}Cu_0Fe_{12}Ni_7$	864 ± 23				
15	$Al_{43}Co_{23}Cr_{21}Cu_0Fe_8Ni_5$	863 ± 34				
16	$Al_{47}Co_{14}Cr_{20}Cu_5Fe_9Ni_5$	859 ± 26				
17	$Co_{14.86}Fe_{14.49}Ni_{15.18}Al_{17.31}Cr_{16.22}Mo_{21.52}Ti_{0.41}$	941 ± 13	857	10	18	This work

2.1. Phase stability and electronic-structure using DFT

To understand the electronic origin, phase stability, elastic moduli, and electronic structure of MPEA1 and MPEA3 with highest and lowest measured hardness (see Table 2) were analyzed. First, the formation energy (E_{form}) of two alloys in BCC, FCC, and HCP phases were calculated. The E_{form} shows that both alloys are stable in bcc phase, i.e., E_{form} (BCC-FCC) is −5.317 mRy/atom for MPEA1 while −4.93 mRy/atom for MPEA3. The hcp phase is not included as E_{form} is more positive, i.e., energetically not stable, compared to BCC or FCC phases. Notably, MPEA1 with higher hardness shows improved stability compared to MPEA3, i.e., E_{form}(MPEA1-MPEA3) = −14 mRy/atom. Furthermore, the comparison between DFT-calculated intrinsic strength (i.e., bulk moduli) and predicted/measured hardness for MPEA1 (246.3 GPa; 930/941 HV) and MPEA3 (201.4 GPa; 761/730 HV) shows good correlation.

Both formation energy and elastic moduli suggest correlation of electronic properties with high hardness of MPEA1. This change in electronic behavior is expected to reflect in electronic structure as well. Therefore, electronic partial density of states (PDOS) for MPEA1 and MPEA3 were plotted in Fig. 9. The overlapping Mo-*4d*, Fe/Co/Ni-*3d* and Al-*3p* PDOS for MPEA1 at −0.20 Ry in Fig. 9(a) shows stronger bonding. While reduced Co and Mo content in MPEA3 (Fig. 9(b)) significantly reduced the bonding of Mo-*4d* and Co-*3d* with other Fe/Ni-*3d* and Al-*3p*, which is also reflected through reduced energy stability and intrinsic strength.

We expect two phase formation due to anti-bonding nature of Cr with other constituents in MPEA1. If we closely look at PDOS below E_{Fermi}, the Cr peaks at −0.15 Ry shows anti-bonding behavior for both MPEA1 and MPEA3, i.e., peaks in Cr PDOS overlaps with valley in Ni/Fe PDOS both for MPEA1 and MPEA3, which works as phase destabilizer for MPEA3 [66]. Our electronic-structure analysis suggests that higher hardness (or strength) of MPEA1 can be attributed to improved stability and increased bonding (reflected in PDOS).

2.2. Microstructural and microchemical characterization

Following ML predictions, electronic-structure analysis and hardness test, detailed microstructural and microchemical characterization were carried out to better understand the observed plastic deformation of MPEA1.

Fig. 10 shows SEM and EDS characterization of GAN-predicted MPEA $Co_{14.86}Fe_{14.49}Ni_{15.18}Al_{17.31}Cr_{16.22}Mo_{21.52}Ti_{0.41}$ with higher hardness than other MPEAs in Table 2. The microstructure (see Fig. 10 (a)) is hypereutectic due to high content of Mo in the alloy. The MPEA is a dual-phase alloy, as substantiates in Fig. 10(b). Dual phases have been cited to be the primary cause for improving mechanical properties like tensile strength [67] and hardness [68] due to finely spaced precipitate interfaces acting as obstructions for dislocation gliding.

To determine the elemental chemistry of bright and dark phases EDS area map, line scan and electron backscattered Kikuchi pattern of bright and dark zones are presented in Fig. 10 (b-h) and Fig. 10 (i-j) respectively. Mo and Cr show high intensity in bright region, which is deficient in Ni and Al. Similarly, the dark phase is abundant in Ni and Al and deficient in Mo and Cr. Cobalt shows only a traceable change in

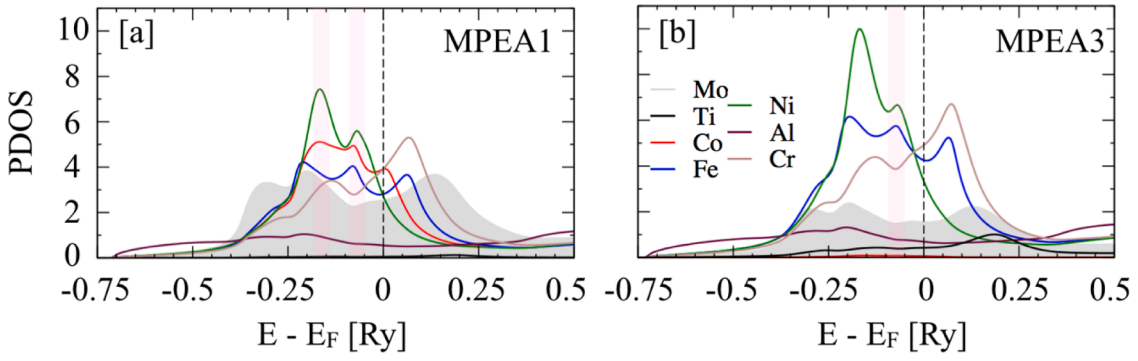

Fig. 9. The partial density of states of (a) MPEA1 ($Co_{14.86}Fe_{14.49}Ni_{15.18}Al_{17.31}Cr_{16.22}Mo_{21.52}Ti_{0.41}$), and (b) MPEA3 ($Co_{0.24}Fe_{20.94}Ni_{19.58}Al_{21.57}Cr_{20.94}Mo_{13.17}Ti_{3.56}$) in bcc phase.

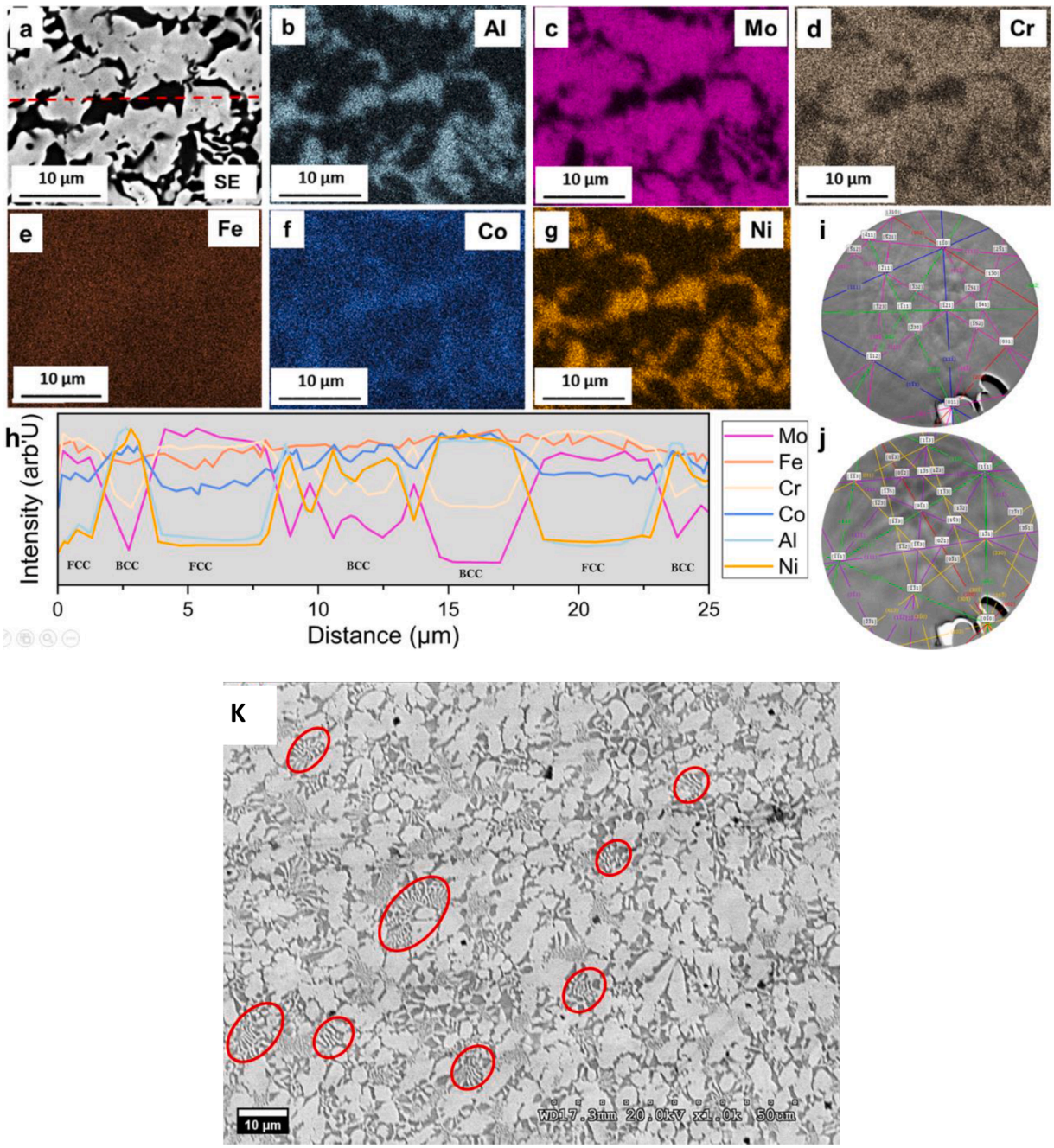

Fig. 10. SEM and EDS analysis of arc-melted $Co_{14.86}Fe_{14.49}Ni_{15.18}Al_{17.31}Cr_{16.22}Mo_{21.52}Ti_{0.41}$ MPEA. (a) Secondary-electron (SE) image, (b) Al, (c) Mo, (d) Cr, (e) Fe, (f) Co, (g) Ni, (h) SE image showing red line segment left to right for EDS mapping, (h) relative intensity vs distance ($\overline{AB}$), suggests Ni-Al-rich dark phase and Mo-Cr rich dark phase, (i), (j) Kikuchi patterns from electron backscattered diffraction (EBSD) point analysis of bright and dark phase, respectively. The Kikuchi pattern shows Miller's indices of diffracting planes and zone axis at intersection of these planes, which suggests that Mo-Cr rich bright phase has a FCC crystal structure and Ni-Al rich dark phase has a BCC crystal structure. (k) Low magnification SEM image of the MPEA with encircled lamellas with a interlaminar spacing of 0.35 ± 0.01 μm. (For interpretation of the references to colour in this figure legend, the reader is referred to the web version of this article.)

intensities in bright and dark regions. However, Fe is found to be uniformly distributed in the two phases. Ti with its very low concentration of 0.0041% is left undetected due to limitations of EDS and matrix effects.

The reason behind grouping of Mo-Cr and Ni-Al can be inferred from the values of ΔH_{mix} (kJ/mol) in Table 4. As Ni and Al have a more negative enthalpy of mixing, they tend to segregate along with Fe and Co in a disordered structure. On the other hand, Mo and Cr have a net zero enthalpy of mixing and hence support solid-solution formation. Fe has an equal enthalpy of mixing with Mo and Ni and hence it is found to be homogeneously distributed. Al and Mo due to their larger atomic radii

Table 4
ΔH_{mix} (kJ/mol) of binary pairs for constituting elements of $Co_{14.86}Fe_{14.49}Ni_{15.18}Al_{17.31}Cr_{16.22}Mo_{21.52}Ti_{0.41}$ MPEA taken from [71].

	Al	Ti	Cr	Fe	Co	Ni
Ti	−30					
Cr	−10	−7				
Fe	−11	−17	−1			
Co	−19	−28	−4	−1		
Ni	−22	−35	−7	−2	0	
Mo	−5	−4	0	−2	−5	−7

and low number of valance electron (3 for Al and 6 for Mo) have been found to improve the mechanical properties of CoCrFeNi alloy system. Al is found to promote the formation of a hard BCC phase on the other hand Mo due to higher Pauling's electronegativity (2.16) and forms extremely hard FCC sigma phases with Cr. The hardness of $Al_xCoCrFeNi$ is found to increase from 120 HV to 527 HV with x increased from 0 to 1 [69]. The hardness of $CoCrFeNiMo_x$ increases from 200 to 900 HV as x increases from 0 to 1 [69,70]. The effect of Al and Mo is altogether captured in this work by GAN model.

The origins of high hardness in the discussed alloy are thought to be multifaceted, ranging from electronic phenomenon resulting in an increased bonding (as reflected by the PDOS in Fig. 9) to microscale phenomena like formation of multiple phases. The microstructure of the MPEA is hypereutectic hence there are fine lamellas scattered in the bulk (Fig. 10(k)) with higher density of MoCrFe-phase. These lamellas increase the phase interface obstructing the dislocation motion and enhancing mechanical properties of the alloy. Supporting examples are found in the works of Dong et al. [72] where the high hardness of AlCrFeNiMo (911.5 HV) was attributed to the presence of primary MoCrFe phase. In alloys with similar constituents, Zhu et al. found that the yield stress for $AlCoCrFeNiMo_{0.5}$ is 2.757 GPa, empirically this is equivalent to a hardness of 8.27 GPa or 898.78 HV [73]. Thus, it is important to note that the CoCrFeNi family of MPEAs without Al and Mo are found to be extremely soft per se, but the addition of Al and Mo induces appreciable hardness into the alloy due to their thermodynamical and lattice effects. Although the electronic effects and phase separation effect may sound totally independent of one another, but, these phenomena are strongly dependent on each other. Ref. [74] investigated the effect of increasing Al content (0–20 at.%) in $(CoCrFeMn)_{(1-x)}Al_x$ and noted a transformation from FCC to BCC separated by a thin duplex region. They pointed out that such phase transitions are driven by thermodynamic linear response quantified by the chemical short-range order. They postulated that the FCC at 0 at.% Al was formed due to the short-range order driven by Co-Cr pair and the BCC at 20% Al was formed due to the Cr-Mn pair. Al played a crucial role in the phase transition with the dual phase region formed due to the Cr-Al short--range order. Their work shows that phase transition arises from electronic origins as reflected in electronic structure calculations, thereby evincing the dependence of phase transformation on electronic effects.

The fact that GAN-predicted MPEA possess the strengthening effects of Al and Mo with microstructure effects, represents the sheer success of the model. The constituents in GAN-predicted MPEAs and the trends in mechanical properties are similar to Zhu et al. [73], however, the measured hardness in our case is superior indicating that the model is able to capture the physics driving strengthening. Although a drawback of our work and most ML works related to hardness predictions is that the predictions are made for holistic hardness of the alloy and not the hardness of a particular phase. Multiple latest reviews like [28,75] on ML on MPEAs have cited lack of inclusion of deformation mechanism, creep mechanism, grain size, and structure, as major drawbacks of ML technique. There are still no methods that can systematically quantify such aspects and include them as descriptors for a large and varied dataset. Properties like hardness and yield strength are numerically measurable and available for a good number of alloys which makes it feasible to use them in ML studies in the form a large, tabulated datasets. But properties like creep and deformation mechanisms or grain structure and sizes are generally not available for each individual alloy system. Therefore, most ML studies are not able to include these aspects as descriptors. And because of inability to include metadata information as descriptors, the predictions are also made in a holistic manner for the entirety of the alloy composition and not with respect to individual phases of the alloys.

3. Conclusions

We presented a unique approach that leverages data analytics in inverse design of MPEAs with high hardness using existing literature data. Our approach permits a multi-dimensional exploration of composition space consisting of chemical, physical, thermodynamical, and atomic descriptors to intricately couple a generative adversarial network (GAN) algorithm with a regressor algorithm (NN). These capabilities were harnessed to design new MPEAs with high hardness using a dataset with 18 elements. More precisely, two alloys with high hardness (one with hardness $>$ 941 HV and another with 858 HV) were discovered and were validated experimentally. The technique demonstrates the capability of GAN to generate new optimized compositions even in a high dimensional space that exhibit a hardness 10% higher than the maximum hardness in the training set. With a large elemental palette there exists an opportunity to optimize compositions for numerous applications ranging from highly corrosion resistant materials to nuclear materials.

Microstructural characterization combined with thermodynamic analysis was carried out in the alloy with the maximum hardness to analyze elemental distributions and understand the origin of improved mechanical response. DFT was used to gain thermodynamic and electronic insights to higher hardness. The calculation shows one-to-one correlation between intrinsic strength (bulk moduli) and ML predicted hardness, which again suggests that GAN was able to accurately capture the underlying physics controlling mechanical response in MPEAs.

Another intriguing aspect to consider is the role of elements present in minor atomic fractions, in determining the hardness of the product alloy. The approach allows a detailed analysis of the impact of compositional variations on hardness and thus serves as a data guided tool for experimentalists to down select their choices for experimental validation of potential candidates. The measured hardness of theoretically predicted MPEAs could be added to the training dataset to enable bootstrapping of the entire workflow and enforce an extrapolation that could possibly lead to significant improvement in model accuracy in property predictions. The bootstrapping effort remains our task targeted for future investigation, although its success will depend more on the number of new data added into the training.

Author contributions

A.R. and A.H. performed ML model construction and data analysis. A.R. drafted the manuscript. M.F.N.T. calculated the features. P.S. performed DFT calculations and analysis. P.Sh. performed microstructural characterization. P.S., G.B., D.D.J. and R.D. oversaw results, discussion, and edited the manuscript. R.D. provided technical expertise on MPEA data, extracted data from research articles, interpreted the results and reviewed the manuscript.

Declaration of Competing Interest

The authors declare that they have no known competing financial interests or personal relationships that could have appeared to influence the work reported in this paper.

Acknowledgments

This effort was principally supported by the U.S. Department of Energy's (DOE) Office of Energy Efficiency and Renewable Energy (EERE) under the Advanced Manufacturing Office (AOP 2.1.0.19) through Ames National Laboratory, which is operated for the U.S. DOE by Iowa State University under contract DE-AC02–07CH11358. This report was prepared as an account of work sponsored by an agency of the United States Government. Neither the United States Government nor any agency thereof, nor any of its employees, makes any warranty, express or implied, or assumes any legal liability or responsibility for the accuracy, completeness, or usefulness of any information, apparatus, product, or process disclosed, or represents that its use would not infringe privately owned rights. Reference herein to any specific

commercial product, process, or service by trade name, trademark, manufacturer, or otherwise does not necessarily constitute or imply its endorsement, recommendation, or favoring by the United States Government or any agency thereof. The views and opinions of authors expressed herein do not necessarily state or reflect those of the United States Government or any agency thereof. The authors acknowledge NSF award (#1944040) for the support to Lehigh on this project.

References

[1] J.W. Yeh, S.K. Chen, S.J. Lin, J.Y. Gan, T.S. Chin, T.T. Shun, C.H. Tsau, S.Y. Chang, Nanostructured high-entropy alloys with multiple principal elements: novel alloy design concepts and outcomes, Adv. Eng. Mater. 6 (5) (2004) 299–303.
[2] B. Cantor, I. Chang, P. Knight, A. Vincent, Microstructural development in equiatomic multicomponent alloys, Mater. Sci. Eng. A 375 (2004) 213–218.
[3] O.N. Senkov, D.B. Miracle, K.J. Chaput, J.P. Couzinie, Development and exploration of refractory high entropy alloys—A review, J. Mater. Res. 33 (19) (2018) 3092–3128.
[4] O.N. Senkov, G. Wilks, J. Scott, D.B. Miracle, Mechanical properties of Nb25Mo25Ta25W25 and V20Nb20Mo20Ta20W20 refractory high entropy alloys, Intermetallics 19 (5) (2011) 698–706.
[5] G. Laplanche, P. Gadaud, O. Horst, F. Otto, G. Eggeler, E. George, Temperature dependencies of the elastic moduli and thermal expansion coefficient of an equiatomic, single-phase CoCrFeMnNi high-entropy alloy, J. Alloy. Compd. 623 (2015) 348–353.
[6] Y. Shi, B. Yang, P.K. Liaw, Corrosion-resistant high-entropy alloys: a review, Metals 7 (2) (2017) 43.
[7] A. Roy, M. Taufique, H. Khakurel, R. Devanathan, D.D. Johnson, G. Balasubramanian, Machine-learning-guided descriptor selection for predicting corrosion resistance in multi-principal element alloys, npj Mater. Degrad. 6 (1) (2022) 1–10.
[8] A. Roy, J. Munshi, G. Balasubramanian, Low energy atomic traps sluggardize the diffusion in compositionally complex refractory alloys, Intermetallics 131 (2021), 107106.
[9] A. Roy, P. Singh, G. Balasubramanian, D.D. Johnson, Vacancy formation energies and migration barriers in multi-principal element alloys, Acta Mater. (2022), 117611.
[10] A. Roy, P. Sreeramagiri, T. Babuska, B. Krick, P.K. Ray, G. Balasubramanian, Lattice distortion as an estimator of solid solution strengthening in high-entropy alloys, Mater. Charact. 172 (2021), 110877.
[11] O. Senkov, J. Miller, D. Miracle, C. Woodward, Accelerated exploration of multi-principal element alloys with solid solution phases, Nat. Commun. 6 (1) (2015) 1–10.
[12] D.B. Miracle, O.N. Senkov, A critical review of high entropy alloys and related concepts, Acta Mater. 122 (2017) 448–511.
[13] D. Miracle, High entropy alloys as a bold step forward in alloy development, Nat. Commun. 10 (1) (2019) 1–3.
[14] A. Roy, R. Devanathan, D.D. Johnson, G. Balasubramanian, Grain-size effects on the deformation in nanocrystalline multi-principal element alloy, Mater. Chem. Phys. 277 (2022), 125546.
[15] A. Sharma, P. Singh, D.D. Johnson, P.K. Liaw, G. Balasubramanian, Atomistic clustering-ordering and high-strain deformation of an Al0. 1CrCoFeNi high-entropy alloy, Sci. Rep. 6 (1) (2016) 1–11.
[16] P. Singh, D. Sauceda, R. Arroyave, The effect of chemical disorder on defect formation and migration in disordered max phases, Acta Mater. 184 (2020) 50–58.
[17] J. Li, Q. Fang, B. Liu, Y. Liu, Y. Liu, Mechanical behaviors of AlCrFeCuNi high-entropy alloys under uniaxial tension via molecular dynamics simulation, RSC Adv. 6 (80) (2016) 76409–76419.
[18] Y. Tang, D. Li, Nano-tribological behavior of high-entropy alloys CrMnFeCoNi and CrFeCoNi under different conditions: a molecular dynamics study, Wear 476 (2021), 203583.
[19] Z. Li, W. Nash, S. O'Brien, Y. Qiu, R. Gupta, N. Birbilis, cardiGAN: a generative adversarial network model for design and discovery of multi principal element alloys, J. Mater. Sci. Technol. 125 (2022) 81–96.
[20] N. Islam, W. Huang, H.L. Zhuang, Machine learning for phase selection in multi-principal element alloys, Comput. Mater. Sci. 150 (2018) 230–235.
[21] J. Rickman, H. Chan, M. Harmer, J. Smeltzer, C. Marvel, A. Roy, G. Balasubramanian, Materials informatics for the screening of multi-principal elements and high-entropy alloys, Nat. Commun. 10 (1) (2019) 1–10.
[22] W. Huang, P. Martin, H.L. Zhuang, Machine-learning phase prediction of high-entropy alloys, Acta Mater. 169 (2019) 225–236.
[23] Y. Qiu, S. Thomas, M.A. Gibson, H.L. Fraser, N. Birbilis, Corrosion of high entropy alloys, npj Mater. Degrad. 1 (1) (2017) 1–18.
[24] K. Kaufmann, K.S. Vecchio, Searching for high entropy alloys: a machine learning approach, Acta Mater. 198 (2020) 178–222.
[25] H. Khakurel, M. Taufique, A. Roy, G. Balasubramanian, G. Ouyang, J. Cui, D. D. Johnson, R. Devanathan, Machine learning assisted prediction of the Young's modulus of compositionally complex alloys, Sci. Rep. 11 (1) (2021) 1–10.
[26] A. Roy, T. Babuska, B. Krick, G. Balasubramanian, Machine learned feature identification for predicting phase and Young's modulus of low-, medium-and high-entropy alloys, Scr. Mater. 185 (2020) 152–158.
[27] A. Roy, I. Roy, L.J. Santodonato, G. Balasubramanian, Data-guided feature identification for predicting specific heat of multicomponent alloys, JOM 74 (2022) 1406–1413.
[28] A. Roy, G. Balasubramanian, Predictive descriptors in machine learning and data-enabled explorations of high-entropy alloys, Comput. Mater. Sci. 193 (2021), 110381.
[29] Y. Zhang, C. Wen, C. Wang, S. Antonov, D. Xue, Y. Bai, Y. Su, Phase prediction in high entropy alloys with a rational selection of materials descriptors and machine learning models, Acta Mater. 185 (2020) 528–539.
[30] Z. Pei, J. Yin, J.A. Hawk, D.E. Alman, M.C. Gao, Machine-learning informed prediction of high-entropy solid solution formation: beyond the Hume-Rothery rules, npj Comput. Mater. 6 (1) (2020) 50.
[31] G. Kim, H. Diao, C. Lee, A. Samaei, T. Phan, M. de Jong, K. An, D. Ma, P.K. Liaw, W. Chen, First-principles and machine learning predictions of elasticity in severely lattice-distorted high-entropy alloys with experimental validation, Acta Mater. 181 (2019) 124–138.
[32] Y.J. Chang, C.Y. Jui, W.J. Lee, A.C. Yeh, Prediction of the composition and hardness of high-entropy alloys by machine learning, JOM 71 (2019) 3433–3442.
[33] C. Wen, Y. Zhang, C. Wang, D. Xue, Y. Bai, S. Antonov, L. Dai, T. Lookman, Y. Su, Machine learning assisted design of high entropy alloys with desired property, Acta Mater. 170 (2019) 109–117.
[34] I.J. Goodfellow, J. Shlens, C. Szegedy, Explaining and harnessing adversarial examples, arXiv preprint (2014).
[35] M. Frid-Adar, I. Diamant, E. Klang, M. Amitai, J. Goldberger, H. Greenspan, GAN-based synthetic medical image augmentation for increased CNN performance in liver lesion classification, Neurocomputing 321 (2018) 321–331.
[36] K. Schawinski, C. Zhang, H. Zhang, L. Fowler, G.K. Santhanam, Generative adversarial networks recover features in astrophysical images of galaxies beyond the deconvolution limit, Mon. Not. R. Astron. Soc. Lett. 467 (1) (2017) L110–L114.
[37] C. Yang, C. Ren, Y. Jia, G. Wang, M. Li, W. Lu, A machine learning-based alloy design system to facilitate the rational design of high entropy alloys with enhanced hardness, Acta Mater. 222 (2022), 117431.
[38] Y. Sun, Z. Lu, X. Liu, Q. Du, H. Xie, J. Lv, R. Song, Y. Wu, H. Wang, S. Jiang, Prediction of Ti-Zr-Nb-Ta high-entropy alloys with desirable hardness by combining machine learning and experimental data, Appl. Phys. Lett. 119 (20) (2021), 201905.
[39] L. Qiao, Z. Lai, Y. Liu, A. Bao, J. Zhu, Modelling and prediction of hardness in multi-component alloys: a combined machine learning, first principles and experimental study, J. Alloy. Compd. 853 (2021), 156959.
[40] S. Li, S. Li, D. Liu, R. Zou, Z. Yang, Hardness prediction of high entropy alloys with machine learning and material descriptors selection by improved genetic algorithm, Comput. Mater. Sci. 205 (2022), 111185.
[41] D. Khatamsaz, B. Vela, P. Singh, D.D. Johnson, D. Allaire, R. Arróyave, Bayesian optimization with active learning of design constraints using an entropy-based approach, npj Comput. Mater. 9 (1) (2023) 49.
[42] B. Vela, C. Acemi, P. Singh, T. Kirk, W. Trehern, E. Norris, D.D. Johnson, I. Karaman, R. Arróyave, High-throughput exploration of the WMoVTaNbAl refractory multi-principal-element alloys under multiple-property constraints, Acta Mater. 248 (2023), 118784.
[43] D.D. Johnson, P. Singh, A. Smirnov, N. Argibay, Universal maximum strength of solid metals and alloys, Phys. Rev. Lett. 130 (16) (2023), 166101.
[44] I. Goodfellow, J. Pouget-Abadie, M. Mirza, B. Xu, D. Warde-Farley, S. Ozair, A. Courville, Y. Bengio, Generative adversarial nets, Adv. Neural Inf. Process. Syst. 27 (2014) 139–144.
[45] K. Wang, C. Gou, Y. Duan, Y. Lin, X. Zheng, F.Y. Wang, Generative adversarial networks: introduction and outlook, IEEE/CAA J. Autom. Sin. 4 (4) (2017) 588–598.
[46] J. Gui, Z. Sun, Y. Wen, D. Tao, J. Ye, A review on generative adversarial networks: algorithms, theory, and applications, IEEE Trans. Knowl. Data Eng. (2021) 3313–3332.
[47] Y. Li, Q. Wang, J. Zhang, L. Hu, W. Ouyang, The theoretical research of generative adversarial networks: an overview, Neurocomputing 435 (2021) 26–41.
[48] J.E. Dayhoff, Neural Network Architectures: an Introduction, Van Nostrand Reinhold Co., 1990.
[49] K. Fukushima, Cognitron: a self-organizing multilayered neural network, Biol. Cybern. 20 (3) (1975) 121–136.
[50] G. Klambauer, T. Unterthiner, A. Mayr, S. Hochreiter, Self-normalizing neural networks, Adv. Neural Inf. Process. Syst. 30 (2017).
[51] A. Nassar, A. Mullis, Rapid screening of high-entropy alloys using neural networks and constituent elements, Comput. Mater. Sci. 199 (2021), 110755.
[52] G. Pharr, W. Oliver, Nanoindentation of silver-relations between hardness and dislocation structure, J. Mater. Res. 4 (1) (1989) 94–101.
[53] C. Chen, A. Hendrickson, Dislocation etch pits in silver, J. Appl. Phys. 42 (6) (1971) 2208–2215.
[54] T.H. Courtney, Mechanical Behavior of Materials, Waveland Press, 2005.
[55] S.M. Lundberg, S.I. Lee, A unified approach to interpreting model predictions, Adv. Neural Inf. Process. Syst. 30 (2017).
[56] D.D. Johnson, D. Nicholson, F. Pinski, B. Gyorffy, G. Stocks, Density-functional theory for random alloys: total energy within the coherent-potential approximation, Phys. Rev. Lett. 56 (19) (1986) 2088.
[57] P. Singh, A. Sharma, A.V. Smirnov, M.S. Diallo, P.K. Ray, G. Balasubramanian, D. D. Johnson, Design of high-strength refractory complex solid-solution alloys, npj Comput. Mater. 4 (1) (2018) 1–8.
[58] J.P. Perdew, K. Burke, M. Ernzerhof, Generalized gradient approximation made simple, Phys. Rev. Lett. 77 (18) (1996) 3865.

[59] Y.F. Zhang, W. Ren, W.L. Wang, N. Li, Y.X. Zhang, X.M. Li, W.H. Li, Interpretable hardness prediction of high-entropy alloys through ensemble learning, J. Alloy. Compd. 945 (2023), 169329.
[60] S. Guo, Phase selection rules for cast high entropy alloys: an overview, Mater. Sci. Technol. 31 (10) (2015) 1223–1230.
[61] M. Wu, R.C. Setiawan, D. Li, Benefits of passive element Ti to the resistance of AlCrFeCoNi high-entropy alloy to corrosion and corrosive wear, Wear 492 (2022), 204231.
[62] Z. Wang, M. Wu, Z. Cai, S. Chen, I. Baker, Effect of Ti content on the microstructure and mechanical behavior of (Fe36Ni18Mn33Al13) 100− xTix high entropy alloys, Intermetallics 75 (2016) 79–87.
[63] G. Qin, R. Chen, H. Zheng, H. Fang, L. Wang, Y. Su, J. Guo, H. Fu, Strengthening FCC-CoCrFeMnNi high entropy alloys by Mo addition, J. Mater. Sci. Technol. 35 (4) (2019) 578–583.
[64] C. Dai, T. Zhao, C. Du, Z. Liu, D. Zhang, Effect of molybdenum content on the microstructure and corrosion behavior of FeCoCrNiMox high-entropy alloys, J. Mater. Sci. Technol. 46 (2020) 64–73.
[65] S. Zhao, Defect properties in a VTaCrW equiatomic high entropy alloy (HEA) with the body centered cubic (bcc) structure, J. Mater. Sci. Technol. 44 (2020) 133–139.
[66] P. Singh, A.V. Smirnov, D.D. Johnson, Ta-Nb-Mo-W refractory high-entropy alloys: anomalous ordering behavior and its intriguing electronic origin, Phys. Rev. Mater. 2 (5) (2018), 055004.
[67] Z. Tang, O.N. Senkov, C.M. Parish, C. Zhang, F. Zhang, L.J. Santodonato, G. Wang, G. Zhao, F. Yang, P.K. Liaw, Tensile ductility of an AlCoCrFeNi multi-phase high-entropy alloy through hot isostatic pressing (HIP) and homogenization, Mater. Sci. Eng. A 647 (2015) 229–240.
[68] A. Shabani, M.R. Toroghinejad, A. Shafyei, R.E. Logé, Microstructure and mechanical properties of a multiphase FeCrCuMnNi high-entropy alloy, J. Mater. Eng. Perform. 28 (4) (2019) 2388–2398.
[69] W.R. Wang, W.L. Wang, S.C. Wang, Y.C. Tsai, C.H. Lai, J.W. Yeh, Effects of Al addition on the microstructure and mechanical property of AlxCoCrFeNi high-entropy alloys, Intermetallics 26 (2012) 44–51.
[70] Y. Liu, Y. Xie, S. Cui, Y. Yi, X. Xing, X. Wang, W. Li, Effect of Mo element on the mechanical properties and tribological responses of CoCrFeNiMo x high-entropy alloys, Metals 11 (3) (2021) 486.
[71] A. Takeuchi, A. Inoue, Classification of bulk metallic glasses by atomic size difference, heat of mixing and period of constituent elements and its application to characterization of the main alloying element, Mater. Trans. 46 (12) (2005) 2817–2829.
[72] Y. Dong, Y. Lu, J. Kong, J. Zhang, T. Li, Microstructure and mechanical properties of multi-component AlCrFeNiMox high-entropy alloys, J. Alloy. Compd. 573 (2013) 96–101.
[73] J. Zhu, H. Fu, H. Zhang, A. Wang, H. Li, Z. Hu, Microstructures and compressive properties of multicomponent AlCoCrFeNiMox alloys, Mater. Sci. Eng. A 527 (26) (2010) 6975–6979.
[74] P. Singh, A. Marshal, A.V. Smirnov, A. Sharma, G. Balasubramanian, K. Pradeep, D. D. Johnson, Tuning phase stability and short-range order through Al doping in (CoCrFeMn) 100− x A l x high-entropy alloys, Phys. Rev. Mater. 3 (7) (2019), 075002.
[75] E.W. Huang, W.J. Lee, S.S. Singh, P. Kumar, C.Y. Lee, T.N. Lam, H.H. Chin, B. H. Lin, P.K. Liaw, Machine-learning and high-throughput studies for high-entropy materials, Mater. Sci. Eng. R Rep. 147 (2022), 100645.